

Electronic Supplementary Information for  
Ultrahigh energy density with excellent thermal stability in lead-free multilayer  
ceramic capacitors *via* composite strategy design

*Peiyao Zhao*<sup>a, †</sup>, *Lingling Chen*<sup>a, †</sup>, *Longtu Li*<sup>a</sup>, *Xiaohui Wang*<sup>a\*</sup>

<sup>a</sup>State Key Laboratory of New Ceramics and Fine Processing, School of Materials  
Science and Engineering, Tsinghua University, Beijing 100084, China

Corresponding Author

**\*Xiaohui Wang, E-mail: wxh@mail.tinghua.edu.cn**

<sup>†</sup>These authors contributed equally to this work.

## Experimental methods

*Fabrication of  $x(\text{Bi}_{0.5}\text{Na}_{0.5})\text{TiO}_3-(1-x)(0.87\text{BaTiO}_3-0.13\text{Bi}(\text{Zn}_{2/3}(\text{Nb}_{0.85}\text{Ta}_{0.15}))_{1/3})\text{O}_3$*

*Ceramics:*  $x(\text{Bi}_{0.5}\text{Na}_{0.5})\text{TiO}_3-(1-x)(0.87\text{BaTiO}_3-0.13\text{Bi}(\text{Zn}_{2/3}(\text{Nb}_{0.85}\text{Ta}_{0.15}))_{1/3})\text{O}_3$

( $x\text{BNT}-(1-x)\text{BTBZNT}$ ) ceramics with compositions of  $x=0.35, 0.4, 0.5,$  and  $0.55$  were prepared by conventional solid-state reaction method using analytical pure grade  $\text{Na}_2\text{CO}_3, \text{TiO}_2, \text{Bi}_2\text{O}_3, \text{ZnO}, \text{BaCO}_3, \text{Nb}_2\text{O}_5,$  and  $\text{Ta}_2\text{O}_5 (>99\%)$  as the starting materials. The  $\text{Na}_2\text{CO}_3, \text{TiO}_2, \text{Bi}_2\text{O}_3$  were weighted according to the nominal stoichiometric compositions and milled in ethanol with zirconia balls for 4 h. After drying, the powder was calcined in an alumina crucible at  $900\text{ }^\circ\text{C}$  for 4 h in air to form BNT ceramic powders. In the similar way, BTBZNT powder was synthesized by  $\text{BaCO}_3, \text{TiO}_2, \text{Bi}_2\text{O}_3, \text{ZnO}, \text{Nb}_2\text{O}_5,$  and  $\text{Ta}_2\text{O}_5$ . Next, weighted powders that consist of BNT and BTBZNT were remilled for 4 h in ethanol. After drying, the powders were granulated with 10 wt% polyvinyl alcohol binder, and compacted into pellets with a diameter of 8 mm and thickness of 1 mm by uniaxial pressing in a stainless-steel die. After the removal of the binder at  $600\text{ }^\circ\text{C}$  for 5 h, the pellets were sintered well in air.

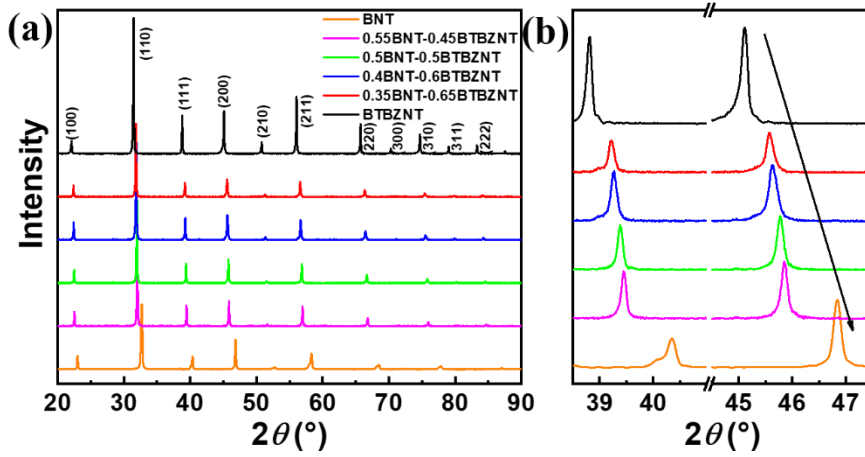
*Fabrication of 0.4BNT-0.6BTBZNT Multilayer Energy Storage Ceramic Capacitors:*

The 0.4BNT-0.6BTBZNT multilayer ceramic capacitors with two active layers were prepared by tape-casting method, where the calcined and high-energy milled 0.4BNT-0.6BTBZNT powder was used as dielectric ceramic material. The weighed powders with dispersant, binder, and plasticizer were milled using zirconia balls for 48 h. The prepared slurry was used to fabricate continuous 0.4BNT-0.6BTBZNT tapes with a thickness of approximately  $10\text{ }\mu\text{m}$  by roll-to-roll tape casting. Then, the tapes screen-

printed with 70Ag/30Pd paste as inner electrodes were stacked layer by layer and precisely aligned with isostatic lamination. After cutting and sintering with two-step sintering schedule (**Fig. S10a**), silver paste was used to terminate the opposite ends of the capacitors and form the outer electrodes for electrical measurements.

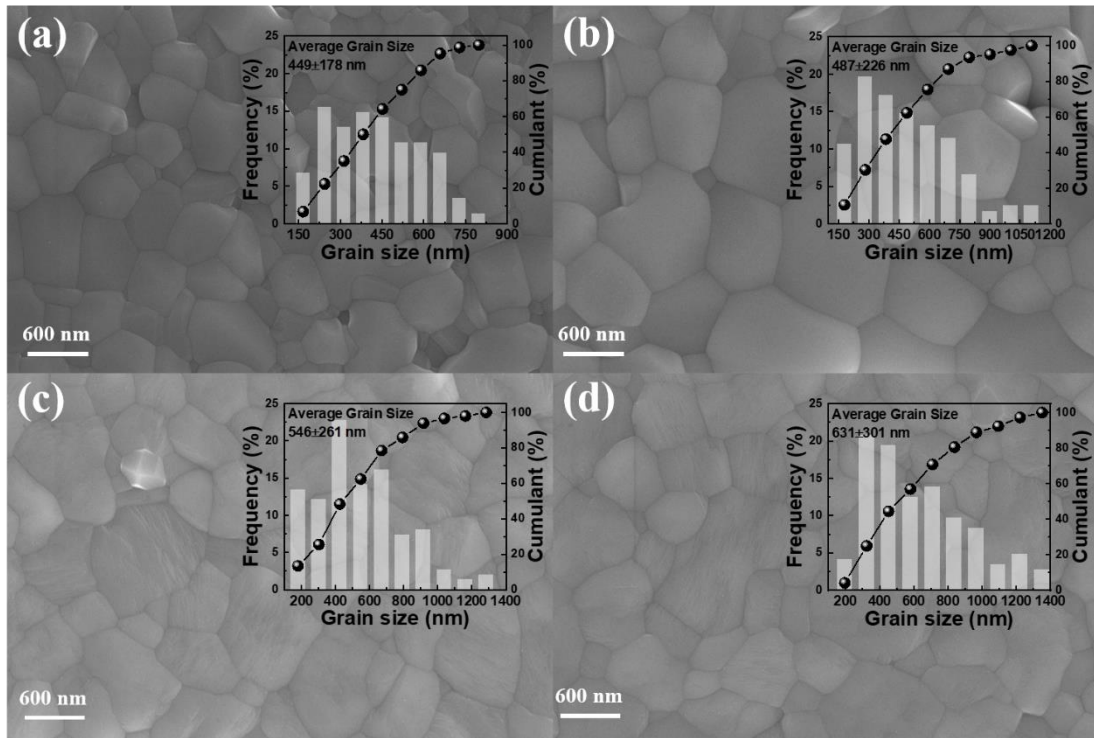
*Characterization of Phase, Microstructure, and Electrical Properties:* Crystalline structures were characterized using X-ray diffraction (Rigaku 2500, Rigaku, Tokyo, Japan) with CuK $\alpha$  radiation ( $\lambda=1.5418 \text{ \AA}$ ). Surface microstructures for the ceramics and multilayer capacitors were observed using a scanning electron microscope (MERLIN VP Compact, Zeiss, Ltd., Germany). Selected area electron diffraction (SAED) and high-resolution transmission electron microscopy (HRTEM) investigations were performed using a field-emission transmission electron microscope (JEM-2010F, JEOL Ltd., Tokyo, Japan), operating at 200 kV. The ceramic pellets were polished down to a thickness of 200  $\mu\text{m}$  and sputtered with Au electrode on both sides of the ceramics for the high electric field measurements. The hysteresis loops were measured with a TF ANALYZER 2000E ferroelectric measurement system at different frequencies (aixACCT Systems GmbH, Aachen, Germany) in the temperature range from 25 to 170  $^{\circ}\text{C}$  with an automated controller (Delta Design 9023, Cohu Semiconductor Equipment Group). The temperature dependence of permittivity was measured in the temperature range of from -55 to 350  $^{\circ}\text{C}$  under the testing condition of 100 Hz to 1 MHz by an impedance analyzer (HP4278A; Hewlett-Packard), with an automated controller (Delta Design 9023, Cohu Semiconductor Equipment Group) at heating rate of 2 $^{\circ}\text{C}/\text{min}$ . The energy release properties of MLCCs were investigated by a charge-discharge platform

(CFD-001, Gogo Instruments Technology, Shanghai, China) with a certain discharge resistance, and capacitance load circuit.



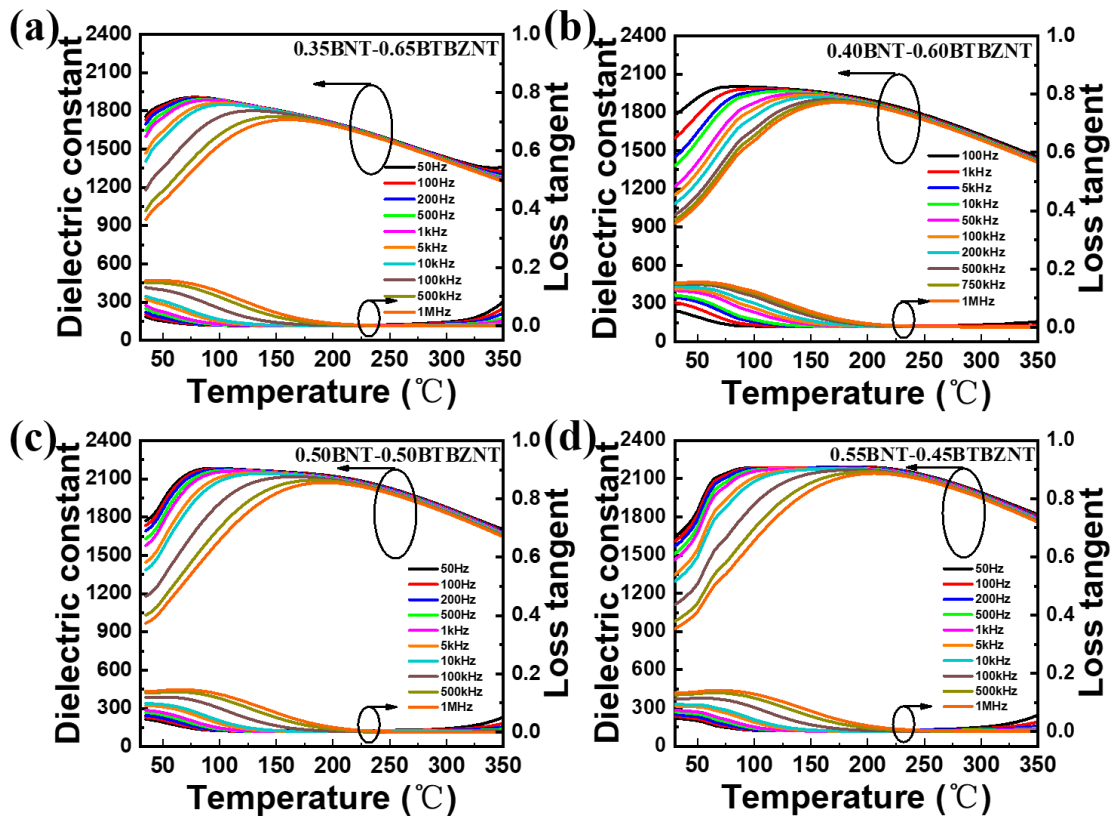
**Figure S1** (a) XRD patterns of the  $x$ BNT-(1- $x$ )BTBZNT ceramics. (b) Magnification of the patterns in (a) from  $38.5^{\circ}$  to  $47.5^{\circ}$ .

Fig. S1(a) shows the XRD pattern of the  $x$ BNT-(1- $x$ )BTBZNT ceramics. As we can see, all the samples exhibit typical perovskite structures without any secondary phase.<sup>1</sup> By enlarging the patterns from  $38.5^{\circ}$  to  $47.5^{\circ}$ , it is clear that no splitting of the (111) and (200) peak can be found in Fig. S1(b), demonstrating that the  $x$ BNT-(1- $x$ )BTBZNT ceramics are mainly a pseudocubic phase at room temperature. Moreover, compared with pure BTBZNT, with the increase of BNT content, the diffraction peaks shift towards higher degrees, which is a symbol of the narrowing interplanar spacing due to the smaller radius of  $\text{Bi}^{3+}$  (1.34 Å) and  $\text{Na}^{+}$  (1.39 Å) than  $\text{Ba}^{2+}$  (1.61 Å).<sup>3,4</sup>



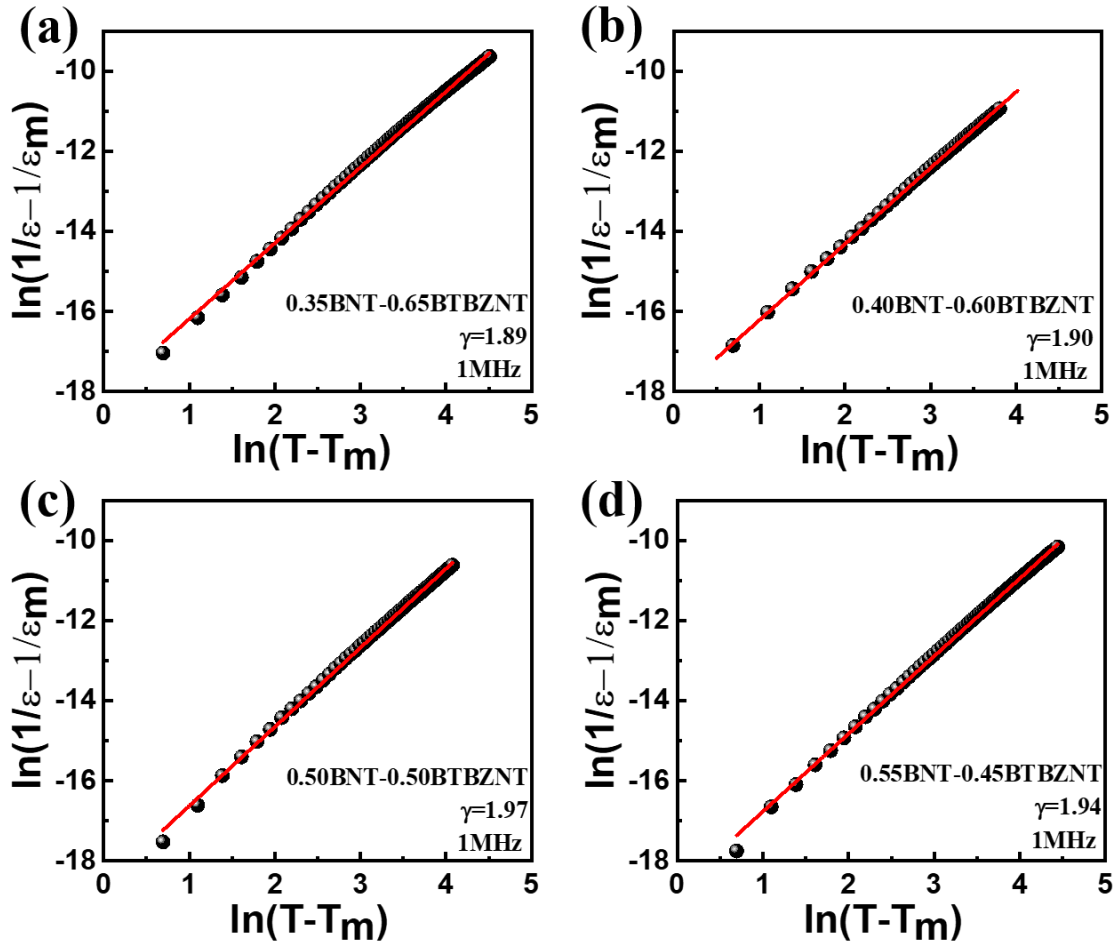
**Figure S2** Microstructure images and grain size distributions for the  $x$ BNT-(1- $x$ )BTBZNT ceramics: (a)  $x=0.35$ , (b)  $x=0.40$ , (c)  $x=0.50$ , (d)  $x=0.55$ .

Fig. S2 gives the typical morphologies of the thermally etched fractured surfaces of the  $x$ BNT-(1- $x$ )BTBZNT ceramics samples. It can be seen that all the four samples are well sintered without any pores, and the average grain size of the samples with BNT content increases from 449 nm to 631 nm.



**Figure S3** Temperature (25 °C to 350 °C) dependence of dielectric constant and loss tangent of  $x\text{BNT}-(1-x)\text{BTBZNT}$  ceramics measured at different frequencies.

The evolution of dielectric properties along with the BNT content increase. As the content of BNT increases, the phase transition from the rhombohedral ( $R$ ) to tetragonal ( $T$ ) phase shifts from below room temperature for 0.35BNT-0.65BTBZNT to 50-75°C for 0.55BNT-0.45BTBZNT. The phase transition from the tetragonal ( $T$ ) to cubic ( $C$ ) phase shifts to high temperature.<sup>5,6</sup>



**Figure S4** Plot of  $\ln(1/\varepsilon - 1/\varepsilon_m)$  as a function of  $\ln(T - T_m)$  of  $x$ BNT-(1- $x$ )BTBZNT ceramics at the frequency of 1 MHz according to the modified Curie-Weiss law. (Symbols: experimental data; solid line: fit).

It is known that the dielectric characteristics of relaxor ferroelectric can be described by the modified Curie-Weiss law:  $1/\varepsilon - 1/\varepsilon_m = (T - T_m)^\gamma/C$ , where  $\varepsilon$  is the dielectric constant at temperature  $T$ ,  $\varepsilon_m$  is the maximum value of dielectric constant, and  $T_m$  is the temperature corresponding to  $\varepsilon_m$ ,  $C$  is the Curie constant, and  $\gamma$  is an indicator of the degree of diffuseness varying from 1 for a normal ferroelectric and 2 for an ideal relaxor ferroelectric.<sup>7,8</sup>  $\ln(1/\varepsilon - 1/\varepsilon_m)$  as a function of  $\ln(T - T_m)$  for  $x$ BNT-(1- $x$ )BTBZNT systems are plotted in Fig. S4 (ESI<sup>†</sup>), from which the  $\gamma$  value can be derived. The  $\gamma$  values were found to be between 1.89 and

1.97 at 1MHz, which manifests the strong relaxation behavior.

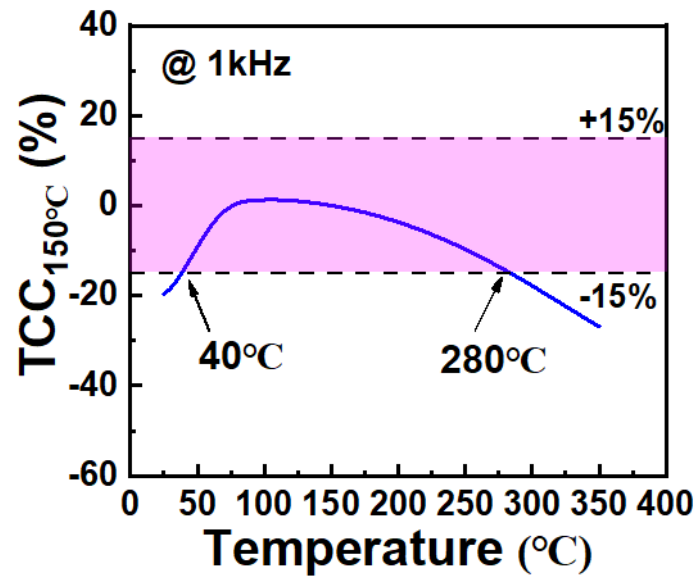


**Figure S5** Temperature coefficient of capacitance ( $TCC_{150^{\circ}\text{C}} = \Delta C/C_{150^{\circ}\text{C}}$ ) curves as a function of temperature measured at 1 kHz for the 0.4BNT-0.6BTBZNT ceramics.

The 0.4BNT-0.6BTBZNT ceramics maintain a  $TCC_{150^{\circ}\text{C}} \leq \pm 15\%$  over a temperature range from 40 to 280 °C at 1 kHz, which shows a good thermal stability. The good thermal stability of dielectric constant leads the MLCCs to possess excellent energy storage properties at high temperature.

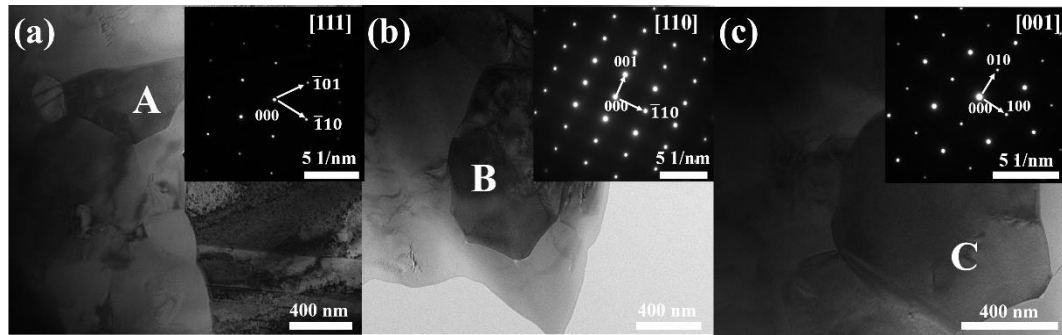


**Figure S6** Bright-field TEM image and the corresponding SAED pattern along (a)  $[111]_c$ , (b)  $[110]_c$  and (c)  $[001]_c$  for 0.4BNT-0.6BTBZNT, respectively. The space group of the 0.4BNT-0.6BTBZNT ceramic is  $P4mm$ .

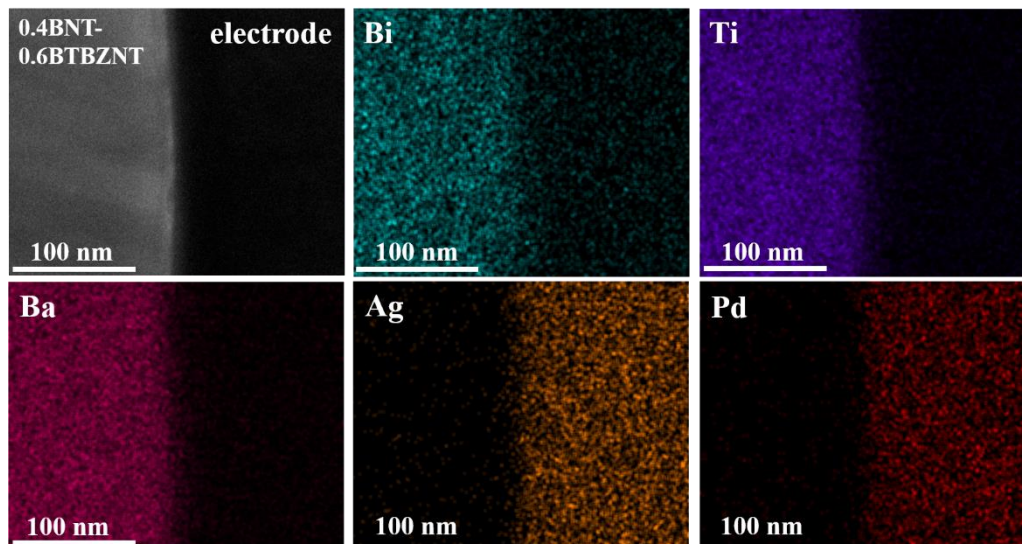


**Figure S7** EDS elements mapping images of the interface between electrodes and dielectric in the 0.4BNT-0.6BTBZNT MLCCs.

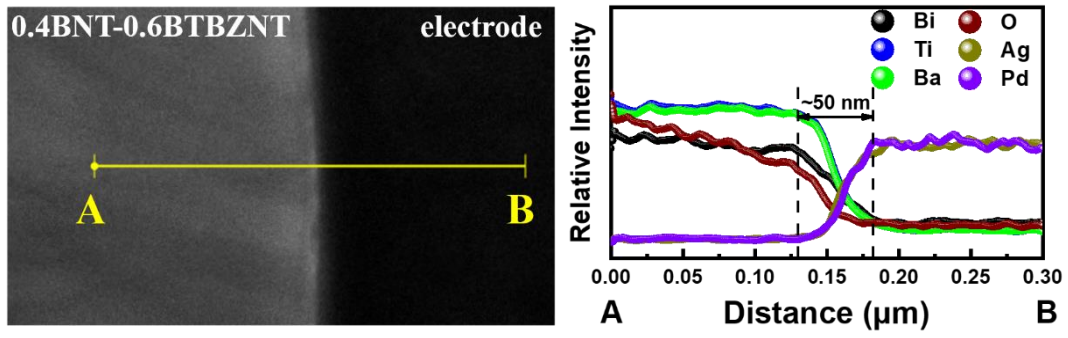


**Figure S8** TEM image of the interface and EDS line profiles of the Bi, Ti, Ba, O, Ag, and Pd distributions along the line in the 0.4BNT-0.6BTBZNT MLCCs.

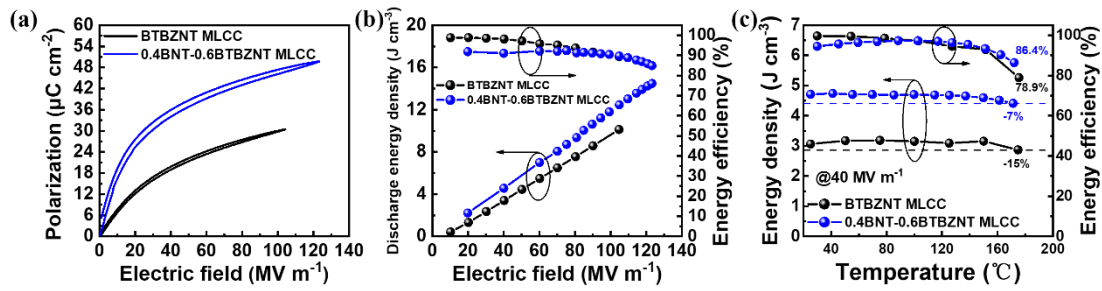


**Figure S9** (a) Unipolar  $P$ - $E$  loops under maximum applied electric field of BTBZNT MLCCs and 0.4BNT-0.6BTBZNT MLCCs measured at room temperature and 10 Hz. (b) The calculated  $U_d$  and  $\eta$  versus applied electric field at room temperature for the BTBZNT MLCCs and 0.4BNT-0.6BTBZNT MLCCs. (c) The calculated  $U_d$  and  $\eta$  measured at  $40 \text{ MV m}^{-1}$  from  $25^{\circ}\text{C}$  to  $\sim 175^{\circ}\text{C}$  for the BTBZNT MLCCs and 0.4BNT-0.6BTBZNT MLCCs. Through composite strategy design, there is a remarkable enhancement on the energy storage performance in 0.4BNT-0.6BTBZNT MLCCs compared with our previous BTBZNT MLCCs, the  $P_{\text{max}}$  and  $U_d$  increased by 63% and 43%, respectively, and the thermal stability at high temperature also enhanced remarkably (see Table S1 for details).

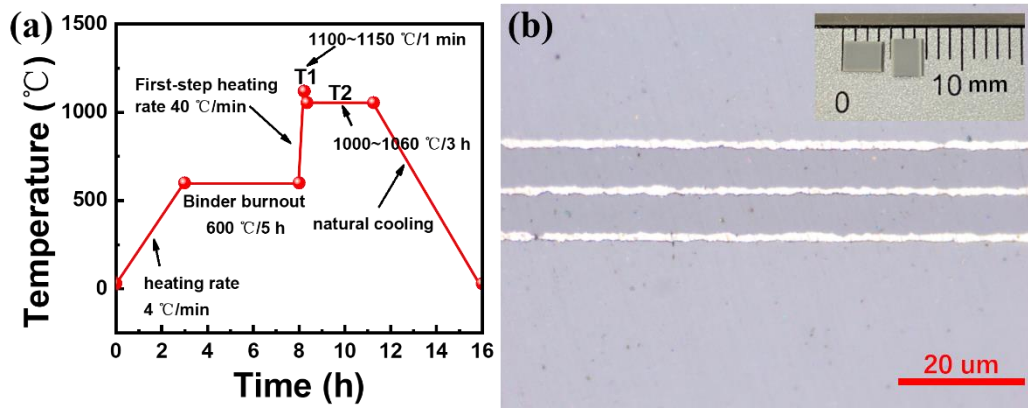


**Figure S10** (a) The two-step sintering heating schedule of 0.4BNT-0.6BTBZNT MLCCs. (b) The optical microscopy image of fabricated 0.4BNT-0.6BTBZNT MLCC. The inset is the image of 0.4BNT-0.6BTBZNT MLCC samples.

**Table S1 Comparisons of BTBZNT MLCCs and 0.4BNT-0.6BTBZNT MLCCs**

Capacitor	$P_{\max}$ ( $\mu\text{C cm}^{-2}$ )	$U_d$ ( $\text{J cm}^{-3}$ )	$\eta(\%)$	Maximum operating temperature ( $^{\circ}\text{C}$ )
BTBZNT <sup>2</sup>	30.4@ 104 MV m <sup>-1</sup>	10.12	89.4	150@40 MV m <sup>-1</sup>
0.4BNT- 0.6BTBZNT	49.7@ 123 MV m <sup>-1</sup>	14.49	84.9	170@40 MV m <sup>-1</sup>

**Table S2 Energy storage performance of various MLCCs**

	Composition	Internal electrode	$E_b$ (MV m <sup>-1</sup> )	$U_d$ (J cm <sup>-3</sup> )	$\eta$ (%)	Ref.
	BTBNT	60Ag/40Pd	45	2.76	84.3	9
BaTiO <sub>3</sub>	BT-BLT	Pt	46.6	4.05	95.5	10
-based	BT-BLN	Pt	45	4.5	91.5	11
	BTBZNT	60Ag/40Pd	104.7	10.12	89.4	2
CaTiO <sub>3</sub>	CTCH	Pt	120	9	93	12
-based	CTCH-Mn	Pt	130	9.6	96	12
PbTiO <sub>3</sub> -based	PBLDZST	5Ag/95Pd	30	3.8	67.4	13
	BNF-BT	Pt	54	6.74	77	14
BiFeO <sub>3</sub>	BF-BST-LMN	Pt	73	10	72	16
-based	BF-BT-NZZ	Pt	70	10.5	87	15
	BF-BT-BLN	Pt	95	13.8	81	18
	BF-ST-BMN	Pt	100	15.8	75.2	19
(Bi <sub>0.5</sub> Na <sub>0.5</sub> )Ti O <sub>3</sub> -based	NBT-SBT	Pt	72	9.5	92	17
0.4BNT- 0.6BTBZNT		70Ag/30Pd	123	14.49	84.9	This work

## Reference

1. E. Aksel, J. S. Forrester, J. L. Jones, P. A. Thomas, K. Page and M. R. Suichomel, *Appl. Phys. Lett.*, 2011, **98**, 152901.
2. P. Zhao, H. Wang, L. Wu, L. Chen, Z. Cai, L. Li and X. Wang, *Adv. Energy Mater.*, 2019, **9**, 1803048.
3. L. Wu, X. Wang and L. Li, *RSC Advances*, 2016, **6**, 14273-14282.
4. M. Zhou, R. Liang, Z. Zhou and X. Dong, *J. Mater. Chem. A*, 2018, **6**, 17896–17904.
5. C. Zhu, Z. Cai, B. Luo, L. Guo, L. Li and X. Wang, *J. Mater. Chem. A*, 2020, **8**, 683-692.
6. C. Zhu, Z. Cai, B. Luo, X. Cheng, L. Guo, Y. Jiang, X. Cao, Z. Fu, L. Li and X. Wang, *ACS Appl. Mater. Interfaces*, 2021, **13**, 28484-28492.
7. Q. Yuan, G. Li, F.-Z. Yao, S.-D. Cheng, Y. Wang, R. Ma, S.-B. Mi, M. Gu, K. Wang, J.-F. Li and H. Wang, *Nano Energy*, 2018, **52**, 203-210.
8. Z. Shen, X. Wang, B. Luo and L. Li, *J. Mater. Chem. A*, 2015, **3**, 18146-18153.
9. L. Chen, H. Wang, P. Zhao, C. Zhu, Z. Cai, Z. Cen, L. Li and X. Wang, *J. Am. Ceram. Soc.*, 2019, **102**, 4178–4187.
10. W.-B. Li, D. Zhou, R. Xu, L.-X. Pang and I. M. Reaney, *ACS Appl. Energy Mater.*, 2018, **1**, 5016-5023.
11. W. Li, D. Zhou, R. Xu, D.-W. Wang, J. Su, L.-X. Pang, W. Liu and G.-H. Chen, *ACS Appl. Energy Mater.*, 2019, **2**, 5499-5506.
12. D. P. Shay, N. J. Podraza, N. J. Donnelly and C. A. Randall, *J. Am. Ceram. Soc.*, 2012, **95**, 1348-1355.
13. L. Chen, N. Sun, Y. Li, Q. Zhang, L. Zhang and X. Hao, *J. Am. Ceram. Soc.*, 2018, **101**, 2313-2320.
14. D. Wang, Z. Fan, D. Zhou, A. Khesro, S. Murakami, A. Feteira, Q. Zhao, X. Tan and Ian M. Reaney, *J. Mater. Chem. A*, 2018, **6**, 4133-4144.
15. G. Wang, Z. Lu, J. Li, H. Ji, H. Yang, L. Li, S. Sun, A. Feteira, H. Yang, R. Zuo, D. Wang and I. M. Reaney, *J. Eur. Ceram. Soc.*, 2020, **40**, 1779-1783.
16. G. Wang, J. Li, X. Zhang, Z. Fan, F. Yang, A. Feteira, D. Zhou, D. C. Sinclair, T. Ma, X. Tan, D. Wang and I. M. Reaney, *Energy Environ. Sci.*, 2019, **12**, 582-588.
17. J. Li, F. Li, Z. Xu and S. Zhang, *Adv Mater*, 2018, **30**, 1802155.
18. G. Wang, Z. Lu, H. Yang, H. Ji, A. Mostaed, L. Li, Y. Wei, A. Feteira, S. Sun, D. C. Sinclair, D. Wang and I. M. Reaney, *J. Mater. Chem. A*, 2020, **8**, 11414-11423.
19. Z. Lu, G. Wang, W. Bao, J. Li, L. Li, A. Mostaed, H. Yang, H. Ji, D. Li, A. Feteira, F. Xu, D. C. Sinclair, D. Wang, S.-Y. Liu and I. M. Reaney, *Energy Environ. Sci.*, 2020, **13**, 2938-2948.